Two- and three-dimensional folding of thin film single-crystalline silicon for photovoltaic power applications

Xiaoying Guo[a,b], Huan Li[c], Bok Yeop Ahn[a,b], Eric B. Duoss[a,b], K. Jimmy Hsia[c,d], Jennifer A. Lewis[a,b], and Ralph G. Nuzzo[a,b,e,1]

[a]Frederick Seitz Materials Research Laboratory, Departments of [b]Materials Science and Engineering, [c]Mechanical Science and Engineering, and [e]Chemistry, and [d]Micro and Nanotechnology Laboratory, University of Illinois, Urbana, IL 61801

Fabrication of 3D electronic structures in the micrometer-to-millimeter range is extremely challenging due to the inherently 2D nature of most conventional wafer-based fabrication methods. Self-assembly, and the related method of self-folding of planar patterned membranes, provide a promising means to solve this problem. Here, we investigate self-assembly processes driven by wetting interactions to shape the contour of a functional, nonplanar photovoltaic (PV) device. A mechanics model based on the theory of thin plates is developed to identify the critical conditions for self-folding of different 2D geometrical shapes. This strategy is demonstrated for specifically designed millimeter-scale silicon objects, which are self-assembled into spherical, and other 3D shapes and integrated into fully functional light-trapping PV devices. The resulting 3D devices offer a promising way to efficiently harvest solar energy in thin cells using concentrator microarrays that function without active light tracking systems.

3D structure | microfabrication | self-folding | photovoltaics | capillary force

Silicon, in crystalline and amorphous forms, is currently used in >90% of the photovoltaic (PV) production, and is likely to increase its dominant position in the foreseeable future (1, 2). Even so, its widespread adoption is limited by fabrication costs (e.g., wafer production accounts for ≈40% of the cost of a module) (3). One attractive strategy to reduce such costs entails the use of ultrathin silicon films as the basic material for solar cells (4–6). Thin film solar cells, however, typically have lower efficiencies due to limited absorption thickness (e.g., for a single-crystalline Si film, a thickness of ≈125 μm is needed to absorb ≈90% of the transmitted light incident on it) (7). To achieve efficient optical absorption, thin-film solar cells need effective strategies to prevent reflective losses as well as light-trapping (LT) mechanisms to enhance the effective optical path length of a cell. This requirement is especially important for silicon due to its high reflectivity, in which >35% of incident photons are reflected from the surface and thereby lost (8), as well as its relatively low absorption cross-section, as an indirect band gap semiconductor (9, 10).

Numerous ideas involving modification of both the front and back surfaces of a Si-based device have been pursued, including the use of textured surface structures (11), antireflection (AR) coatings (12), and LT schemes (13, 14). Recently, more complex designs have been explored to improve LT efficiency through the use of various 3D architectures (15–19), including V-folded thin film organic solar cells (17, 18), 3D thin film cadmium telluride (CdTe) solar cells deposited over the top of carbon nanotube tower arrays (15, 19), spherical devices, although from solid Si spheres (16), and cylindrical-shaped solar cells (Solyndra Inc.) made of a thin film of copper indium gallium selenium (CIGS) deposited on a glass tube. These designs are able to increase the optical path length through multiple internal and external reflections to enhance light absorption within an optically thin semiconductor absorber. Also, unlike conventional flat solar cells, such 3D optical structures can absorb light efficiently from a wide range of incident directions.

The creation of electronic devices with 3D form factors is challenging due in part to the inherently planar nature of wafer-based fabrication methods. The most practical methods currently employ planar microfabrication techniques, followed by other processes that transform planar objects into the desired 3D structures (20, 21). Whereas microelectronics rely on stacking and interconnecting individual layers (22), folding and self-assembly routes are attracting increasing attention as an alternative approach to 3D microfabrication (23). To date, folded 3D structures have been obtained through the use of magnetic forces (24), residual stresses (25), and electrical activation (26). Capillary forces may also be harnessed to guide the assembly of 3D, submillimeter scale objects (27–29). However, the relationship between residual stresses (such as those found in epitaxial thin films) and these interfacial driving forces that guide material deformation during self-assembly are not fully understood.

Here, we exploit the mechanical bendability of thin, single-crystalline Si foils of a few micrometers in thickness, coupled with capillary-driven, self-assembly to create folded 3D PV devices. These flexible constructs readily lend themselves to adopting nonplanar shapes, such as triangular prisms, cylinders, and spheres, with less defects than would result from the deformation of thicker Si wafers (30, 31). The resulting 3D functional architectures inherently serve as a LT element allowing for a substantial improvement in efficiency relative to its planar analogues.

Results and Discussion

Folding of Thin Si Foils. Fig. 1*A* schematically shows the basic steps to fabricate a free-standing thin single-crystalline silicon film, which serves as the generic planar precursor to a specifically folded object. In the first step (Fig. 1*A Top*), photolithography is used to define a resist layer with the geometric shape of the intended free-standing Si foil, followed by etching to remove the exposed Si. These resist structures carry a square array of holes (≈2.5-μm diameter, and ≈40-μm pitch) that facilitate undercutting of the foil from a Si-on-insulator (SOI) wafer. Removing the resist with acetone and then etching the buried oxide (BOX)
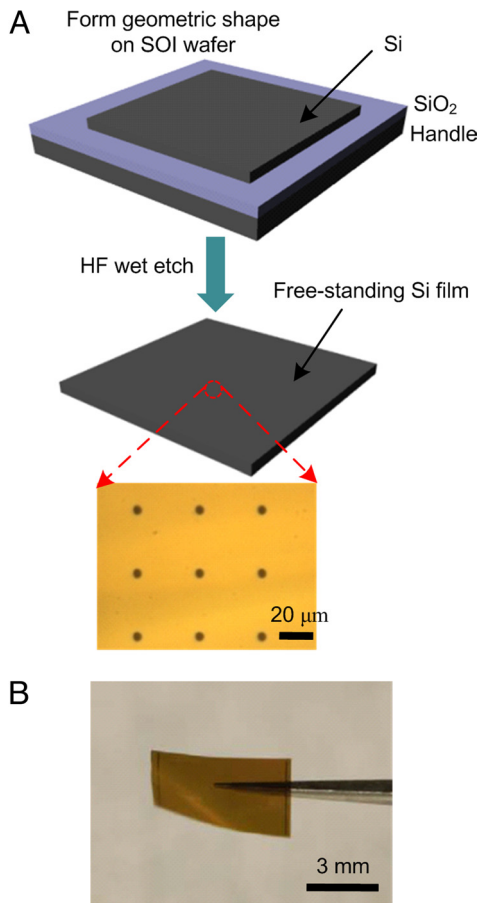
Fig. 1. Fabrication of a free-standing thin Si film from an SOI wafer. (*A*) Schematic representation of the fabrication. (*B*) Optical image of a square silicon membrane (6 × 6 mm) with thickness of 1.25 μm suspended from tweezers.

Fig. 2. Spontaneously folding of (*A*) triangular and (*B* and *C*) square silicon sheets (1.25 μm thick) with a water droplet.

layer with concentrated hydrofluoric acid (HF) releases the top Si film from the underlying Si handle wafer. The thickness of the top Si on the SOI wafer defines the foil thickness. Although fragile, this foil can be manipulated, as shown in Fig. 1*B* for a prototypical square Si film (6 mm × 6 mm, 1.25 μm thick) held by tweezers. The thin silicon foil can be reversibly bent to a relatively small radius of curvature, if the maximum stress in the foil does not exceed the tensile strength of silicon. For a free-standing 2-μm-thick Si foil, this maximum stress will reach the material's tensile strength at a bending radius of curvature of ≈40 μm (32).

During the folding experiment, a Si foil with a specific geometric shape, thickness, and size is placed on a hydrophobic Teflon surface. A droplet of water is placed at the center of the foil. For reasons discussed in detail below, the volume of the water droplet needs to be large enough so that the water-Si-air triple junction line reaches and pins near the corners of the foil. As water evaporates, the capillary forces at the receding water-silicon-air triple junction pulls the corners of the Si sheet up, causing it to wrap around the water droplet with a specific form directed by mechanics considerations. This phenomenon is illustrated by the time-lapse images of folding of a triangular- and two square-shaped foils shown in Fig. 2. For both the triangular and square Si foils (1.25 μm thick), the initial folding is symmetric, with all corners bending toward the center of the sheet. Such behavior is similar to that observed for polydimethylsiloxane (PDMS) sheets (28). As the water evaporates further, the triangular sheet eventually folds into a hollow tetrahedral pyr-
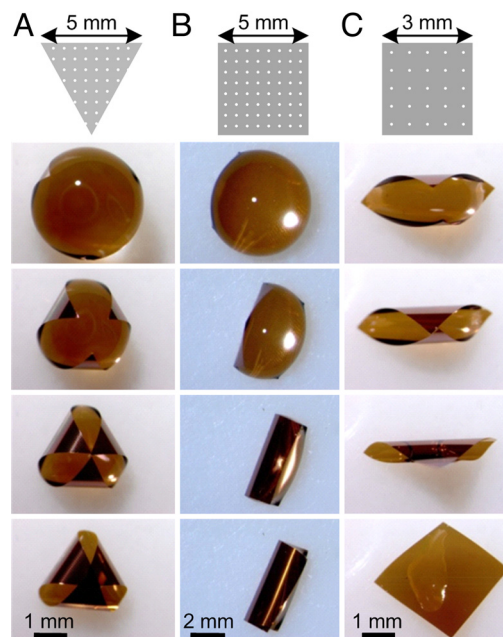
amid (Fig. 2*A*). By contrast, because the symmetric folding eventually becomes unstable for square sheets, they adopt one of two possible modes of cylindrical deformation as shown in Fig. 2 *B* and *C*. Both of these folded states possess high symmetry, as discussed below. Last, when the water droplet fully evaporates, the folded Si foils reopen to adopt their natural, flat shape unless other methods are used to retain the folded shape, as desired for the construction of 3D PV devices.

Critical Folding Criteria. To deterministically produce self-assembled 3D structures, one needs to understand the driving force and the governing parameter(s) for the folding process. Qualitatively, it is imagined that, as the water droplet volume decreases, the increase of strain energy due to folding is balanced by the decrease of surface energy. The surface tension γ thus competes with the bending stiffness B to determine whether a given foil will undergo a folding transition. For both triangular and square sheets (Fig. 2), folding starts with the bending at the corners, which is the necessary condition for the thin sheet to achieve its final folded state and a starting point for the quantitative analysis described below.

To explain the folding process and identify its governing parameters, a mechanics model has been developed. The basic hypothesis of the model is that the driving force for bending of the thin foil is provided by the capillary interaction at the triple junction. Each corner of the thin sheet is modeled as a tapered cantilever beam (Fig. 3*A*). We consider that the capillary force acts on the beam at location $x = L_p$ with a magnitude $P = \gamma t$, where γ is the surface tension, and t is the length of the contact line (or width of the beam) at L_p. To bend the Si sheet, this force must be sufficient to overcome the bending resistance of the beam.

Using the Bernoulli beam theory (33), the governing differential equation for a tapered beam under small deflection is given by

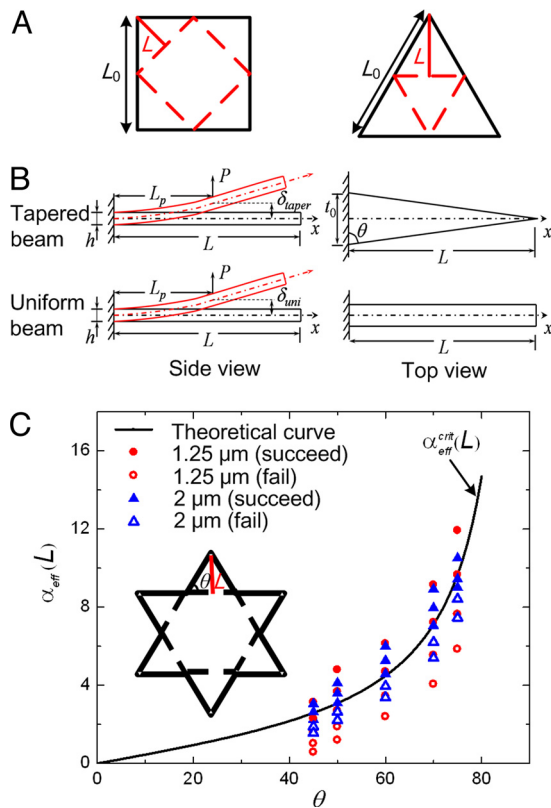$$B_x \frac{d^2w}{dx^2} = P(L_p - x) \qquad [1]$$

Fig. 3. Mechanics model. (*A*) Schematic representation of the symmetry lines (dotted lines) as the fixed ends during folding for both square and triangular sheets. (*B*) Equivalence between the tapered beam and the uniform beam: The external force *P* applied at the same location $x = L_p$ results in the same displacement $\delta_{taper} = \delta_{uni}$ (δ is the deflection at the location of triple junction L_p); (*C*) Critical α_{eff} for folding vs. shape (θ). (*Inset*) Shape design, *L* is the measured beam length and θ is chosen to be 45°, 50°, 60°, 70°, 75°. Solid line, prediction curve from the model; red circles, measured α_{eff} for folding of 1.25-μm-thick Si sheets; blue triangles, measured α_{eff} for folding of 2-μm-thick Si sheets.

where *w* is the deflection, *P* is the external force exerted at the position $x = L_p$, $B_x = (1 - x/L)Et_0h^3/12(1 - \nu^2)$ is the local bending stiffness, with *E* being the Young's modulus, ν the Poisson's ratio, t_0 the width at the beam end, and *h* the beam thickness. To examine the bending behavior of a tapered beam with any base angle θ (Fig. 3*B*), one needs to find the equivalence between a tapered beam and a beam of simple geometry. Here, we assume that if the deflections of a tapered beam and a uniform beam are equal at location $x = L_p$ ($\delta_{taper} = \delta_{uni}$), as shown in Fig. 3*B*, then these two beams are considered "equivalent." The equivalence condition leads to an effective bending stiffness B_{eff}, comprised of the bending stiffness B_0 of uniform beam with width t_0, and a nondimensional function $f(\xi)$, where $\xi = L_p/L$ is the location of the fluid-solid junction line. A nondimensional parameter $\alpha_{eff} = \gamma_{eff}L_p^3/B_{eff}$, with $\gamma_{eff} = \gamma_0(1 - \xi)$ and γ_0 the surface tension, which characterizes the competition between an effective capillary force and the effective bending resistance, can be defined. At the critical position $\xi = \xi_c = L_p^{crit}/L$, α_{eff} reaches its maximum value, given by

$$\alpha_{eff}^{crit} = 0.816 \frac{\gamma_0 L^2}{E'h^3} \cdot \tan\theta \qquad [2]$$

where $E' = E/(1 - \nu^2)$ is the plane strain Young's modulus, and θ denotes the base angle, shown in Fig. 3*B*. Eq. **2** shows that the

nondimensional parameter α_{eff}^{crit} consists of two dimensionless parts, an intrinsic material parameter

$$\alpha_{int} = 0.816 \frac{\gamma_0 L^2}{E'h^3} \qquad [3]$$

that is related to the material properties and characteristic dimensions of the structure, and a shape factor $S(\theta) = \tan\theta$, which is related to the angle θ only.

The mechanics model predicts that, if folding is governed by this nondimensional parameter, then once a combination of the materials and shape parameters reaches a critical value folding will occur. For any given material, the intrinsic nondimensional materials parameter given by Eq. **3** is a constant, which can be determined by a single experiment. With this parameter at hand, the folding of foils of different shapes can be predicted solely by the shape factor.

We experimentally measured the intrinsic nondimensional parameter α_{int} in Eq. **3** using a thin Si foil of uniform cross-section (Fig. S1). The critical length of *L* is found to be 0.9 mm for a 1.25-μm-thick Si membrane, giving rise to the intrinsic value of $\alpha_{int} = 2.59$. We note that this nondimensional value should be applicable to thin Si foils of any thickness and length, and can be used to determine the critical conditions for folding of a tapered foil of any angle. The critical nondimensional parameter of any tapered beam of angle θ can therefore be expressed by

$$\alpha_{eff}^{crit}(\theta) = 2.59 \tan\theta \qquad [4]$$

Eq. **4** plotted as the solid curve in Fig. 3*C* represents a master curve for folding of a tapered foil of any angle. We measured the critical α_{eff}^{crit} at folding of the star-shaped foil with five different angles θ (Fig. 3*C Inset*). The experimental data are shown in Fig. 3*C* together with the master curve of Eq. **4**. In Fig. 3*C*, solid symbols represent the cases in which complete folding is observed, whereas open symbols represent the cases in which the foil failed to fold. Here, the boundary between the open and solid symbols gives the locus of the critical nondimensional parameter governing the folding process. Fig. 3*C* clearly shows that the measured results agree extremely well with the model prediction. The only deviation occurs at $\theta = 45°$, which may arise from symmetry limitations of the folding process. This value, $\theta = 45°$, corresponds to a square-shaped foil, which, after the initial symmetric folding from all four corners, will fold from either the two opposing corners or the two opposing edges, as shown in Fig. 2 *B* and *C*. Either folding pattern will render longer folding characteristic lengths, thus a smaller value of the nondimensional parameter than that predicted by Eq. **4**.

Three-Dimensional PV Devices. Using the mechanics model to predict design dimensions, we created 3D PV devices from thin, single-crystalline Si foils. Fig. 4*A* schematically illustrates the steps for fabricating a 3D Si solar cell, which via assembly adopts the form of a thin spherical shell. This architecture embraces many compromises that serve to simplify the fabrication requirements, although at the expense of ultimate device performance. The process begins with defining of a flower pattern with lateral dimensions beyond the critical folding condition defined by the mechanical modeling. In this demonstration, we used a leaflet fabricated using a SOI wafer (2 μm thick, *p*-type device top, 10–20 Ω cm), additional processing/doping steps to create rectifying transverse pn junctions, and thin metal contact pads. The spacing between n$^+$ and p$^+$ regions in the surface layer is set at 50 μm; this spacing provides a high internal electrical field to efficiently separate photogenerated electron-hole pairs. The flower-shaped planar device layer is released from the Si substrate and placed onto a Teflon substrate with the top surface
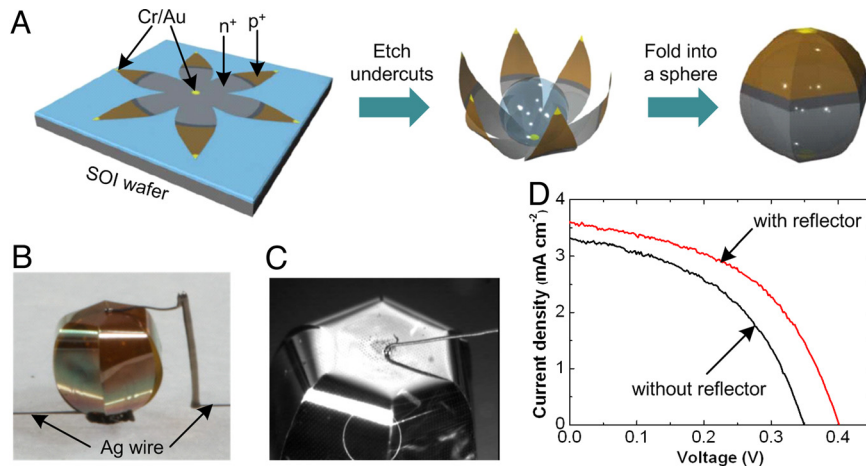
Fig. 4. Spherical solar cells self-assembled from flower-shaped flat Si leaflets with thicknesses of 2 μm. (*A*) Schematic representation of steps for fabricating a spherical-shaped Si solar cell. (*B*) Optical image of a complete device consisting of the folded spherical Si shell, inner glass bead, and printed silver electrodes. (*C*) Magnified view of the silver wire connected to the top contact of the spherical device. (*D*) Current density (*J*)–voltage (*V*) characteristics of a spherical solar cell under AM 1.5 simulated sunlight irradiation, with and without a white diffuse reflector.

(face with the metal contact pads) facing downwards. The image sequence provided in Fig. S2 shows the precise folding of the Si foil into the expected (nearly) spherical shape. To retain the desired spherical shape after the water drop has fully evaporated, we placed a glass bead coated with an adhesive poly(vinyl alcohol) (PVA) layer at the center of the flower pattern to "freeze" the 3D structure in place, once it has reached its desired folded state. Last, a direct-write metallization process (34) is used to make electrical Ag-wire contacts to the bottom and top side contact pads (see *SI Materials and Methods*). Fig. 4 *B* and *C* shows a completely wired spherical device on a glass substrate and a close-up view of the top Ag-wire contact, respectively.

To ascertain the quality of the deformed 3D Si devices, current-voltage measurements of individual solar cells are made at room temperature in the dark and with a solar simulator set at 100 mW/cm^2 and air mass (AM) 1.5 direct filter. Fig. 4*D* shows *J–V* characteristics recorded for a typical spherical Si solar cell with and without a back-side reflector. The solar cell area, defined as the projected surface area of a sphere, is ≈0.05 cm^2. Without the reflector, this spherical cell shows a short-circuit current density, J_{sc}, of 3.31 mA/cm^2, an open-circuit voltage, V_{oc}, of 351 mV, and a fill factor (FF) of 0.47 for an overall conversion efficiency of 0.56%.

This device, although functional, is one of relatively low performance from the perspective of Si-based devices. The relatively poor performance is a result of the fabrication processes, which are not optimized. Among these, the performance is most affected by the elimination of the high temperature process needed to provide a back-surface doping field. Given its absence, the high surface area to volume ratio strongly accelerates losses due to recombination. The high recombination is evidenced by the low V_{oc} of the folded 3D device and the high diode ideality factor of 2 (Fig. S3*B*) (35). To enhance the short circuit current density (J_{sc}), an antireflective coating would also be needed to minimize the surface reflection loss. Also, the metal contacts used for this foil are not optimal choices for PV devices (for a more complete analysis, see *SI Materials and Methods*). As might be expected, process modification unrelated to the folding steps can enhance performance; this improvement is illustrated by the data in Fig. S4, which shows *J–V* characteristics from an on-wafer Si solar device with the same doping profile, but having a layer of SiO$_2$ (100 nm) deposited on the surface and thicker metal contacts (Cr/Au, 10/100 nm). The measured efficiency in this case reaches 2%, which is comparable

with other transverse and vertical junction thin film Si solar cells with comparable dimensions (36–38).

An interesting property of the spherical device is illustrated by the data presented in the top *J–V* curve of Fig. 4*D*, which shows the effects of a diffuse white reflector (Al) on the electrical performance of the cell. We find that the values of J_{sc}, V_{oc} and FF increase to 3.60 mA/cm^2, 401 mV and 0.49, respectively. The addition of a diffuse reflector leads to a 41.1% increase in the conversion efficiency, which is consistent with the prediction of Minemoto's theory (16).

Spherical PV devices constructed from thin solar cells are attractive, because they embed an intrinsic LT form factor (39–41). Their spherical light-receiving surface also intrinsically serves as a passive tracking optic, accepting light from all directions. Nevertheless, the elegance of this 3D architecture is offset by the complexity of the fabrication processes needed to construct it. The "flower-like" form required for guided self-assembly does not "tile" the planar wafer; thus, its Si content is not effectively used.

To overcome the above limitations, we examined 3D LT architectures that simplify the fabrication/assembly processes, can be efficiently tiled on planar surfaces, and are compatible with non-SOI sources (6, 42–45). Specifically, we explored a simpler 3D structure composed of a cylindrical solar cell. Fig. 5*A* schematically illustrates the flat square solar cell design, including dimensions and doping profiles. The planar precursor used consists of Boron-doped (L_{p+} = 0.5 mm), phosphorus-doped (L_{n+} = 5.4 mm), and undoped (L_p = 0.1 mm) regions. Two metal contacts (Cr/Au, 3/50 nm thick, 100 μm wide) are formed onto the n$^+$ and p$^+$ regions, respectively. This structure is fabricated on a SOI wafer with a 3 μm thick, p-type (10–30 Ω cm) device top. As noted above, both sourcing and thickness of the device can be easily varied by substituting a bulk Si (111) wafer with a suitably modified process flow (6). Fig. 5*B* shows a cylindrical solar cell made by folding a flat Si device, with the dimensions (Fig. 5*A*) lying beyond the critical lengths as deduced from the mechanics model, around a PVA-coated cylindrical rod (diameter, 2 mm) through the evaporation of water. The rod in turn was fabricated from a liquid, photocurable polymer (NOA73; Norland) by replica molding.

Representative *J–V* measurements from a square Si solar cell sheet and the cylindrical device folded from the same sheet under AM 1.5 illumination are shown in Fig. 5*D*. The cell area in this case is defined as the projection area of the cylindrical
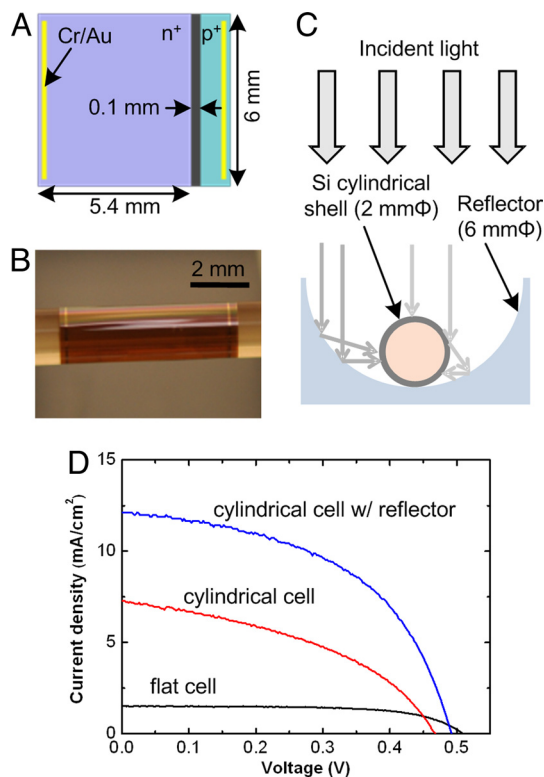
Fig. 5. Doping layout and electrical performance of a cylindrical Si solar cell with a thickness of 3 μm. (*A*) Dimensions and doping profiles of the flat square device. (*B*) Optical image of a cylindrical device mounted on a cylindrical lens. (*C*) Schematic representations of a cylindrical silicon solar cell with a reflector system (cross-sectional structure). (*D*) J–V curves under AM 1.5 illumination from a flat cell and a cylindrical cell self-assembled from the same flat sheet.

device (12 mm^2). The flat cell has an open circuit voltage of 507 mV, a short circuit current of 1.51 mA/cm^2, a FF of 0.65, and the overall conversion efficiency of 0.52%. The cylindrical cell has an open circuit voltage of 467 mV, a short circuit current of 7.26 mA/cm^2, a FF of 0.42, and most notable, the overall conversion efficiency increases to 1.49%. As compared with the planar configuration, the J_{sc} and efficiency are found to increase by 381 and 187%, respectively. The 8% decrease in V_{oc} is attributable to the large A_{pn}/A_L ratio (A_{pn} is the p-n junction area, A_L is the light irradiation area). In our case, A_{pn} can be regarded as the surface area of n$^+$ region (5.4 × 6 mm), and A_L is the projection area of the cylinder (2 × 6 mm). Therefore, the A_{pn} is 2.7 times larger than A_L (for the flat Si solar cell, A_{pn}/A_L ratio is 0.9, 5.4 × 6 mm^2/6 × 6 mm^2). The larger value A_{pn}/A_L increases the saturation current density J_o, which is the dominant parameter leading to the reduction of V_{oc} (16). This inherent decrease in V_{oc} can be remediated by adding a diffuse white reflector. Fig. 5*C* schematically shows the cross-sectional view of a cylindrical Si solar cell integrated with a semiconcentration reflector system. The reflector has ≈3× light concentration ratio, defined here as the ratio of the aperture area of the reflector (6 × 6 mm) to the projection area of the cylinder, resulting in a reduced A_{pn}/A_L ratio of 0.9. As shown in the top J–V curve in Fig. 5*D*, the V_{oc} of the cylindrical cell with reflector increased to 494 mV, a value close to that of the flat cell. The design of the reflector shown is one that is able to improve J_{sc} by collecting reflected light coming from near the edge of the cylinder. In contrast to the flat solar cells, the incident angles (θ) of lights are not always normal to the substrate ($\theta = 0°$), varying significantly at different positions on the surface of a cylindrical-shaped solar cell (from 0° at the center to 90° at the edge, as shown in Fig. 5*C*). The

cylindrical-shaped reflector mitigates reflective losses of this type and substantially improves the performance of the cell. The J–V results shown in Fig. 5*D* in fact demonstrate a maximum output power with the reflector that is ≈2.1 times larger than that without it. However, this enhancement is still somewhat smaller than the expectation based on the geometrical concentration factor and suggests further improvements can be made. Even so, we obtain a higher total output power from the cylindrical cell (0.363 mW) than that from a flat sheet with the same thickness (0.182 mW) and an equivalent mass. This observation strongly validates the LT competency of this 3D structure.

Conclusions

This work describes a strategy for fabricating 3D single crystalline Si structures through a combination of photolithography and self-folding driven by capillary interactions, and suggests a route to 3D LT architecture for use in PV applications. We have constructed spherical and cylindrical-shaped Si solar cells and evaluated their improved electrical performances and competencies for LT and mitigation of reflective losses. We believe 3D structures of this type can be combined easily with other LT/guiding principles (46) to generate device form factors that are low-cost, simple, yet capable of high efficiency performance. This work also identifies the conditions under which folding of the patterned thin foil occurs, and provides a mechanics model that fully predicts the critical conditions for folding for thin foils with complicated shapes. The intrinsic, nondimensional material parameter defined in the model is one that can be generalized to essentially any solid material, as well as diverse shapes and sizes. We believe extensions can be made to other exemplary forms of functional assembly as well as to driving forces not involving the simple mechanisms of capillary forces exploited in the current work.

Materials and Methods

Fabrication of Thin Si Films. The starting material is a SOI wafer (Ultrasil) with a *p*-type device layer (thickness between 100 nm and 3 μm) and a BOX layer (thickness between 400 nm and 4 μm). Spin casting, exposing (365 nm light, through a Karl Suss MJB3 Mask Aligner) and developing a layer of photoresist (AZ5214, Clariant; developer, AZ351, Clariant) formed a pattern that defines the geometric shape of the thin Si foil. Reactive-ion etching (PlasmaTherm 790 series) using SF$_6$ [40 standard cubic cm/min (s.c.c.m.), 30 mTorr, 100 W, etch rate 200 nm/min] removed the exposed parts of the top silicon. After removing the resist with acetone, concentrated HF (Fisher, 49% concentration) was deposited over the patterned surface to remove the BOX and undercut the platelet. Immersing the etched sample into a water tank released the top thin Si film from the host wafer.

Fabrication of 3D Solar Cells. The fabrication process began with a SOI wafer (*p*-type, Boron doped device layer, 2–3 μm thick, 10–20 Ω cm, 4-μm-thick BOX; Ultrasil) that was coated with a layer of SiO$_2$ (400 nm) formed by plasma-enhanced chemical vapor deposition (PECDV) at 250 °C. Photolithography defined the lateral dimensions of the planar solar cells (flower or square shapes), followed by etching the SiO$_2$ not protected by the photoresist and the underlying Si by buffered oxide etchant (6:1 Transene) and reactive-ion etching, respectively. Selective area doping of top contacts was then conducted using liquid sources of boron (p$^+$) spin-on glass (SOG) dopant (B153; Filmtronics) and phosphorus (n$^+$) SOG dopant (P8545SF; Filmtronics), heating at 1,000 °C under N$_2$ atmosphere for 60 min (boron) and 30 min (phosphorus). A layer of SiO$_2$ (600 nm) deposited by PECVD at 250 °C was patterned by photolithography and etched in buffered oxide etchant to serve as a doping mask. The doped wafer was then cleaned and coated with metal electrodes that were defined by photolithography and lift-off. An electron-beam (Temescal, FC 1800) evaporate ion source was used to deposit the metal Cr (3 nm) and Au (50 nm) metal layer. The device surface was patterned with a square hole array (≈2.5-μm diameter, ≈40-μm pitch), and the exposed Cr/Au and Si were removed with commercial etchants (Transene) and a SF$_6$ plasma, respectively. After releasing the top Si layers in HF, the planar sheets were folded into the intended 3D-structured solar cells (spherical or cylindrical shapes) embedding a size-matched lens inside.

1. Maycock P (2003) PV market update. *Renew Energ World* 6:84–101.
2. Smestad GP, Lampert CM (2007) Solar power 2006, San José, CA. *Sol Energy Mater Sol Cells* 91:440–444.
3. Brendel R (2004) Thin-film crystalline silicon mini-modules using porous Si for layer transfer. *Sol Energy* 77:969–982.
4. Green MA, et al. (2004) Crystalline silicon on glass (CSG) thin-film solar cell modules. *Sol Energy* 77:857–863.
5. Green MA (2004) Recent developments in photovoltaics. *Sol Energy* 76:3–8.
6. Yoon JS, et al. (2008) Ultrathin silicon solar microcells for semitransparent, mechanically flexible and microconcentrator module designs. *Nat Mater* 7:907–915.
7. Tsakalakos L (2008) Nanostructures for photovoltaics. *Mater Sci Eng R* 62:175–189.
8. Nakajima K, Ohdaira K, Fujiwara K, Pan WG (2005) Solar cell system using a polished concave Si-crystal mirror. *Sol Energy Mater Sol Cells* 88:323–329.
9. Kovalev D, et al. (2000) Optical absorption cross sections of Si nanocrystals. *Phys Rev B* 61:4485–4487.
10. Marsh AC, Inkson JC (1986) Scattering matrix theory of transport in heterostructures. *Semoncond Sci Technol* 1:285–290.
11. Lipinski M, et al. (2002) Double porous silicon layer on multi-crystalline Si for photovoltaic application. *Sol Energy Mater Sol Cells* 72:271–276.
12. Zhou WD, Tao M, Chen L, Yang HJ (2007) Microstructured surface design for omnidirectional antireflection coatings on solar cells. *J Appl Phys* 102:103105.
13. Obermeyer P, Haase C, Stiebig H (2008) Advanced light trapping management by diffractive interlayer for thin-film silicon solar cells. *Appl Phys Lett* 92:181102.
14. Zeng L, et al. (2006) Efficient enhancement in Si solar cells by textured photonic crystal back reflector. *Appl Phys Lett* 89:111111.
15. Camacho RE, et al. (2007) Carbon nanotube arrays for photovoltaic applications. *JOM* 59:39–42.
16. Minemoto T, et al. (2006) Design strategy and development of spherical silicon solar cell with semi-concentration reflector system. *Sol Energy Mater Sol Cells* 90:3009–3013.
17. Rim SB, et al. (2007) An effective light trapping configuration for thin-film solar cells. *Appl Phys Lett* 91:243501.
18. Andersson V, Tvingstedt K, Inganas O (2008) Optical modeling of a folded organic solar cell. *Appl Phys Lett* 103:094520.
19. Flicker J, Ready J (2008) Simulations of absorbance efficiency and power production of three dimensional tower arrays for use in photovoltaics. *J Appl Phys* 103:113110.
20. Xia Y, Whitesides GM (1998) Soft lithography. *Angew Chem Int Ed* 37:550–575.
21. Gates BD, et al. (2004) Unconventional nanofabrication. *Annu Rev Mater Res* 34:339–372.
22. Gandghi SK (1994) in *VLSI Fabrication Principles* (Wiley, New York), p 728.
23. Whitesides GM, Boncheva M (2002) Beyond molecules: Self-Assembly of mesoscopic and macroscopic components. *Proc Natl Acad Sci* 99:4769–4774.
24. Boncheva M, et al. (2005) Magnetic self-assembly of three-dimensional surfaces from planar sheets. *Proc Natl Acad Sci* 102:3924–3929.
25. Li XL (2008) Strain induced semiconductor nanotubes: From formation process to device applications. *J Phys D Appl Phys* 41:193001.
26. Jager EWH, Smela E, Inganas O (2000) Microfabricating conjugated polymer actuators. *Science* 290:1540–1545.
27. Bruzewicz DA, et al. (2006) Biomimetic fabrication of 3D structures by spontaneous folding of tapes. *J Am Chem Soc* 128:9314–9315.
28. Py C, et al. (2007) Capillary origami: Spontaneous wrapping of a droplet with an elastic sheet. *Phys Rev Lett* 98:156103.
29. Boncheva M, Whitesides GM (2005) Templated self-assembly: Formation of folded structures by relaxation of pre-stressed, planar tapes. *Adv Mater* 17:553–557.
30. Nakajima K, Fujiwara K, Pan WG (2005) Hemisphere-shaped silicon crystal wafers obtained by plastic deformation and preparation of their solar cells. *J Electron Mater* 34:1047–1052.
31. Nakajima K, Fujiwara K, Pan WG, Okuda H (2005) Shaped silicon-crystal wafers obtained by plastic deformation and their application to silicon-crystal lenses. *Nat Mater* 4:47–50.
32. Petersen KE (1982) Silicon as a mechanical material. *Proc IEEE* 70:420–457.
33. Gere JM, Timoshenko S (1997) in *Mechanics of Materials* (PWS Pub. Co., Boston), 4th Ed, pp 599–604.
34. Ahn BY, et al. (2009) Omnidirectional printing of flexible, spanning, and stretchable silver microelectrodes. *Science* 323:1590–1593.
35. Green MA (1982) in *Solar Cells: Operating Principles* (Prentice-Hall Inc., Englewood Cliffs, NJ), pp 274.
36. Liang ZC, Shen H, Xu NS, Reber S (2003) Characterisation of direct epitaxial silicon thin film solar cells on a low-cost substrate. *Sol Energy Mater Sol Cells* 80:181–193.
37. Takato H, Yui N, Hayashi Y, Sekigawa T (1994) Charateristics of three-μm-thick silicon solar cells using bonded silicon-on-insulator wafer. *Jpn J Appl Phys* 33:L1396–L1398.
38. Kasai H, Wada H, Matsumura H (2001) Performance of 6 μm thick crystalline silicon solar cells on glass substrate. *Sol Energy Mater Sol Cells* 65:533–539.
39. Liu ZX, et al. (2007) A concentrator module of spherical Si solar cell. *Sol Energy Mater Sol Cells* 91:1805–1810.
40. Maruyama T, Minami H (2003) Light trapping in spherical silicon solar cell module. *Sol Energy Mater Sol Cells* 79:113–124.
41. Bisconti R, Ossenbrink HA (1997) Optical modelling of silicon solar cells in spherical shape. *Sol Energy Mater Sol Cells* 48:1–6.
42. Ko HC, Baca A, Rogers JA (2006) Bulk quantities of single-crystal silicon micro/nanoribbons generated from bulk wafers. *Nano Lett* 6:2318–2324.
43. Mack S, et al. (2006) Mechanically flexible thin-film transistors that use ultrathin ribbons of silicon derived from bulk wafers. *Appl Phys Lett* 88:213101.
44. Baca AJ, et al. (2007) Printable single-crystal silicon micro/nanoscale ribbons, platelets and bars generated from bulk wafers. *Adv Funct Mater* 17:3051–3062.
45. Baca AJ, et al. (2008) Semiconductor wires and ribbons for high-performance flexible electronics. *Angew Chem Int Ed* 47:5524–5542.
46. Goetzberger A, Goldschmidt JC, Peters M, Löper P (2008) Light trapping, a new approach to spectrum splitting. *Sol Energy Mater Sol Cells* 92:1570–1578.